Spin-Density Distribution, Conformation, and Hydrogen Bonding of the Redox-Active Tyrosine Y_Z in Photosystem II from Multiple Electron Magnetic-Resonance Spectroscopies: Implications for Photosynthetic Oxygen Evolution

Cecilia Tommos,[†,‡] Xiao-Song Tang,[§] Kurt Warncke,[‡,⊥] Curtis W. Hoganson,[‡] Stenbjörn Styring,[†] John McCracken,[‡] Bruce A. Diner,*[,§] and Gerald T. Babcock*[,‡]

Contribution from the Department of Biochemistry, Arrhenius Laboratories for Natural Science, Stockholm University, S-10691 Stockholm, Sweden, Department of Chemistry, Michigan State University, East Lansing, Michigan 48824, and Central Research and Development Department, Experimental Station, E. I. Du Pont de Nemours and Company, Wilmington, Delaware 19880-0173

Received June 5, 1995[⊗]

Abstract: The oxidized form of the redox-active Y_Z tyrosyl residue involved in photosynthetic oxygen evolution has been generated and trapped in Mn-depleted Photosystem II core complexes from a D2-Y160F mutant strain of *Synechocystis* 6803. This system eliminates interference from P_{700}^+ and $Y_D^\bullet$ and allowed characterization of $Y_Z^\bullet$ by using a combination of specific ^2H-labeling and electron magnetic-resonance techniques that included CW-EPR, frequency-modulated and transient detected ENDOR, and ^2H-ESEEM. Using these complementary techniques, we have carried out a detailed evaluation of the hyperfine structure of $Y_Z^\bullet$ and obtained the dipolar interactions to weakly coupled nuclei, the strongly anisotropic tensors of the ring-hydrogens, and the more isotropic interactions to the β-methylene site. No ^2H_2O exchangeable features could be detected by CW-ENDOR, implying that Y_Z is not involved in a well-ordered hydrogen bond in its radical form. From the hyperfine coupling tensors the spin-density distribution of $Y_Z^\bullet$ was derived with the following values: C_1 (0.37), $C_{2,6}$ (−0.07), $C_{3,5}$ (0.26), and C_4−O (0.25). These values are similar to those reported for other tyrosyl radicals, both hydrogen bonded and non-hydrogen bonded. We conclude that tyrosyl radicals are not tuned to specific function by large-scale modulations of their spin density through hydrogen-bonding effects. ENDOR and ^2H-ESEEM spectra representing the hyperfine interactions of the β-methylene site provided evidence of rotational mobility about the tyrosyl C_1-C_β bond. A quantitative analysis of the ^2H-ESEEM data provided a distribution in θ of about 14°. The observation of mobility in the Y_Z site, and the lack of a well-ordered hydrogen bond are inconsistent with the conventional view of Y_Z as a pure electron-transfer component in Photosystem II. Rather, we suggest a hydrogen-atom transfer function for Y_Z in water oxidation. Within this model, the $(Mn)_4/Y_Z$ center forms the Oxygen-Evolving Complex of Photosystem II where the $(Mn)_4$ cluster binds substrate water and delocalizes oxidizing equivalents and Y_Z acts by abstracting hydrogens from substrate water in either a concerted or sequential fashion.

Introduction

The Photosystem II/oxygen-evolving complex (PSII/OEC) catalyzes the light-induced oxidation of water to molecular oxygen in higher plants, algae, and cyanobacteria. Scheme 1 conveys the conventional view of the redox components and chemistry involved.[1] The water-splitting reactions are driven by the oxidizing power created by the light-induced oxidation of the PSII reaction center chlorophyll, P_{680}. The oxidizing equivalents generated at P_{680}^+ are transferred to the $(Mn)_4$ cluster, which is integral in forming the catalytic site of the OEC, by the oxidation and re-reduction of a nearby tyrosyl residue, Y_Z, identified by site-directed mutagenesis as tyrosine 161 on the D1 reaction center protein.[2] Within this scheme, Y_Z plays a critical role in facilitating the high quantum efficiency

Scheme 1

$$\underbrace{(Mn)_4\,2H_2O}_{\text{Oxygen-Evolving Complex}} \xrightarrow{e^-} \underbrace{Y_Z}_{\text{charge-transfer interface}} \xrightarrow{e^-} \underbrace{P_{680}}_{\text{photo-chemistry}}$$

with which water oxidation occurs. By re-reducing P_{680}^+ in the sub-microsecond time range, it effectively outcompetes the deleterious recombination reaction between P_{680}^+ and the reduced quinone acceptor, Q_A^-. Moreover, because the reduction potentials of tyrosyl radicals are high, typically 1 V, Y_Z oxidation preserves the redox instability generated by P_{680}^+ formation that is necessary to oxidize water. The four manganese ions in the OEC provide binding sites for substrate water, accumulate the four oxidizing equivalents required for the water-oxidizing reactions, and are thought to be essential in the formation of the oxygen−oxygen bond.[3] During the water-oxidizing process, the $(Mn)_4$ cluster cycles through five different redox states, which are designated S_0 to S_4; oxygen is evolved as S_4 is reduced to S_0. Calcium and chloride ions are also

[†] Stockholm University.
[‡] Michigan State University.
[§] E. I. Du Pont de Nemours and Company.
[⊥] Present address: Department of Physics, Emory University, Atlanta, GA 30322.

[⊗] Abstract published in *Advance ACS Abstracts,* October 1, 1995.

(1) (a) Andersson, B. A.; Styring, S. In *Current Topics in Bioenergetics;* Lee, C. P.; Academic Press: San Diego, 1991; Vol. 16, pp 1−81. (b) Seibert, M. In *The Photosynthetic Reaction Center;* Deisenhofer, J., Norris, J. R., Eds.; Academic Press: San Diego, 1993; Vol. I, pp 319−356. (c) Diner, B. A.; Babcock, G. T. In *Oxygenic Photosynthesis: The Light Reactions;* Ort, D., Yocum, C., Eds.; Kluwer: Dordrecht, 1995; in press.

(2) (a) Debus, R. J.; Barry, B. A.; Sithole, I.; Babcock, G. T.; McIntosh, L. *Biochemistry* **1988**, *27*, 9071−9074. (b) Metz, J. G.; Nixon, P. J.; Rögner, M.; Brudvig, G. W.; Diner, B. A. *Biochemistry* **1989**, *28*, 6960−6969.

(3) Yachandra, V. K.; DeRose, V. J.; Latimer, M. J.; Mukerji, I.; Sauer, K.; Klein, M. P. *Science* **1993**, *260*, 675−679.

0002-7863/95/1517-10325$09.00/0

required for oxygen evolution, and several essential polypeptides have been identified.[4]

The oxidizing side of PSII contains a second redox-active tyrosyl residue, Y_D, symmetrically positioned relative to Y_Z at Y161 (Y160 in *Synechocystis*) on the D2 protein.[5] Y_D has kinetic[6,7] and thermodynamic[7,8] properties that differ from those of Y_Z[8,9] and is not located in the main route of electron transfer in PSII; thus far, the biological significance of Y_D remains unknown.

The functional differentiation observed for Y_Z and Y_D implies the existence of structural differences, either between the radicals themselves or in their local protein environments. For the Y_D radical, spectroscopic characterization has been favored by its slow redox kinetics. Detailed studies have provided the electron spin-density distribution and geometry of the radical,[10,11] shown the existence of a hydrogen bond to the phenol oxygen,[12,13] rendered evidence of low mobility at the Y_D site,[11,14] and, in combination with site-directed mutagenesis, probed the local protein environment of the radical.[13,15,16]

In contrast, the fast redox reactions of Y_Z have made this species more difficult to study. Originally, Y_Z was detected by EPR in thylakoid membranes in which the reduction of the radical had been slowed by the removal of the $(Mn)_4$ cluster.[17] The EPR line shape of $Y_Z^\bullet$ under oxygen-evolving conditions could be obtained by using time-resolved techniques.[18,19] The overall hyperfine structure of $Y_Z^\bullet$ in the intact O_2-evolving system was shown to be similar, if not identical, to that in the Mn-depleted material and, moreover, very similar to the line shape of $Y_D^\bullet$, which has been interpreted to indicate similar electron spin-density distribution patterns between the two radicals.[19] However, the $Y_Z^\bullet$ and $Y_D^\bullet$ electron paramagnetic resonance (EPR) line shapes are not identical and small differences have been reported.[20,21] Computational studies have predicted differences in the immediate environments and hydrogen-bonding status of Y_Z and Y_D.[22,23] There is conflicting evidence concerning the disorder, and even the existence, of a hydrogen bond to $Y_Z^\bullet$.[14,21,24] Thus, despite the central role of Y_Z in the water-oxidation process, our understanding of its physical properties and of its interactions with its local protein environment is rudimentary. Obtaining deeper insight into these issues has been hampered by the transient nature of the radical, by the relatively low spin concentrations that can be obtained in PSII preparations, and by EPR spectral overlap with the more stable P_{700}^+ and $Y_D^\bullet$ species. As a consequence, it has not been possible to assess the spectroscopic and functional properties of $Y_Z^\bullet$ within the developing understanding of the behavior of functionally essential tyrosyl radicals that occur in a variety of enzymes.[25]

In the work presented here, we have addressed these problems by generating and trapping $Y_Z^\bullet$ at low temperatures in Mn-depleted PSII core complexes from a Y_D-less mutant strain of *Synechocystis* 6803.[21] The system has been investigated by using a combination of specific ^2H-labeling and a variety of electron magnetic-resonance techniques. Resolution and sensitivity difficulties that limit the usefulness of continuous-wave EPR and frequency-modulated electron nuclear double resonance (ENDOR) in characterization of the samples have been overcome by using transient-detected ENDOR and ^2H electron spin-echo envelope modulation (^2H-ESEEM) spectroscopy. With these complementary techniques, we provide a detailed evaluation of the hyperfine structure of $Y_Z^\bullet$ that provides information on unpaired electron spin-density distribution, conformation, rotational mobility, and hydrogen-bonding status of the Y_Z radical. Our results indicate that the role of Y_Z in water oxidation is likely to extend beyond the simple electron-transfer function depicted in Scheme 1.

Materials and Methods

Growth Conditions and Sample Preparation. D2-Y160F mutant cells of *Synechocystis*[21] were grown photoautotropically in 18-L carboys in BG-11 medium.[26] The carboys were bubbled with 5% CO_2 in air at 30 °C under constant illumination for 5−6 days. For isotopic labeling experiments, D2-Y160F mutant cells were grown photoautotropically in BG-11 medium containing 0.5 mM phenylalanine, 0.25 mM tryptophan, and 0.25 mM specifically ^2H-labeled tyrosine for 6−7 days following the method of Barry and Babcock.[27]

PSII core complexes from *Synechocystis* 6803, depleted of the $(Mn)_4$ cluster, were prepared according to a modification of the procedure

(4) (a) Yocum, C. F. *Biochim. Biophys. Acta* **1991**, *1059*, 1−15. (b) Debus, R. J. *Biochim. Biophys. Acta* **1992**, *1102*, 269−352. (c) Boussac, A.; Rutherford, A. W. *Biochem. Soc. Trans.* **1994**, *22*, 352−358.

(5) (a) Debus, R. J.; Barry, B. A.; Babcock, G. T.; McIntosh, L. *Proc. Natl. Acad. Sci. U.S.A.* **1988**, *85*, 427−430. (b) Vermaas, W. F. J.; Rutherford, A. W.; Hansson, Ö. *Proc. Natl. Acad. Sci. U.S.A.* **1988**, *85*, 8477−8481. (c) Koulougliotis, D.; Tang, X.-S.; Diner, B. A.; Brudvig, G. W. *Biochemistry*, **1995**, *34*, 2850−2856.

(6) (a) Babcock, G. T.; Sauer, K. *Biochim. Biophys. Acta* **1973**, *325*, 483−503. (b) Messinger, J.; Renger, G. *Biochemistry* **1993**, *32*, 9379−9386.

(7) Vass, I.; Styring, S. *Biochemistry* **1991**, *30*, 830−839.

(8) Boussac, A.; Etienne, A.-L. *Biochim. Biophys. Acta* **1984**, *766*, 576−581.

(9) (a) Babcock, G. T.; Blankenship, R. E.; Sauer, K. *FEBS Lett.* **1976**, *61*, 286−289. (b) Brettel, K.; Schlodder, E.; Witt, H. T. *Biochim. Biophys. Acta*, **1984**, *766*, 403−415. (c) Dekker, J. P.; van Gorkom, H. J.; Brok, M.; Ouwehand, L. *Biochim. Biophys. Acta* **1984**, *764*, 301−309. (d) Dekker, J. P.; Plijter, J. J.; Ouwehand, L.; van Gorkom, H. J. *Biochim. Biophys. Acta* **1984**, *767*, 176−179. (e) Rappaport, F.; Blanchard-Desce, M.; Lavergne, J. *Biochim. Biophys. Acta* **1994**, *1184*, 178−192.

(10) (a) Hoganson, C. W.; Babcock, G. T. *Biochemistry* **1992**, *31*, 11874−11880. (b) Rigby, S. E. J.; Nugent, J. H. A.; O'Malley, P. J. *Biochemistry* **1994**, *33*, 1734−1742.

(11) Warncke, K.; Babcock, G. T.; McCracken J. *J. Am. Chem. Soc.* **1994**, *116*, 7332−7340.

(12) (a) Rodriguez, I. D.; Chandrashekar, T. K.; Babcock, G. T. In *Progress in Photosynthesis;* Biggins, J., Ed.; Martinus Nijhoff Publishers: Dordrecht, **1987**; Vol. I, pp 119−133. (b) Evelo, R. G.; Dikanov, S. A.; Hoff, A. J. *Chem. Phys. Lett.* **1989**, *157*, 25−30. (c) Evelo, R. G.; Hoff, A. J.; Dikanov, S. A.; Tyryshkin, A. M. *Chem. Phys. Lett.* **1989**, *161*, 479−484.

(13) Tang, X.-S.; Chisholm, D. A.; Dismukes, G. C.; Brudvig, G. W.; Diner, B. A. *Biochemistry* **1993**, *32*, 13742−13748.

(14) Mino, H.; Kawamori, A. *Biochem. Biophys. Acta* **1994**, *1185*, 213−220.

(15) Tommos, C.; Davidsson, L.; Svensson, B.; Madsen, C.; Vermaas, W.; Styring, S. *Biochemistry* **1993**, *32*, 5436−5441.

(16) Tommos, C.; Madsen, C.; Styring, S.; Vermaas, W. *Biochemistry* **1994**, *33*, 11805−11813.

(17) Babcock, G. T.; Sauer, K. *Biochim. Biophys. Acta* **1975**, *376*, 315−328.

(18) Blankenship, R. E.; Babcock, G. T.; Warden, J. T.; Sauer, K. *FEBS Lett.* **1975**, *51*, 287−293.

(19) Hoganson, C. W.; Babcock, G. T. *Biochemistry* **1988**, *27*, 5848−5855.

(20) (a) Kodera, Y.; Takura, K.; Mino, H.; Kawamori, A. In *Research in Photosynthesis;* Murata, N., Ed.; Kluwer Academic Publishers: Dordrecht, 1992; Vol. II, pp 57−60. (b) Boerner, R. J.; Barry, B. A. *J. Biol. Chem.* **1993**, *268*, 17151−17154.

(21) Tang, X.-S.; Zheng, M.; Chisholm, D. A.; Dismukes, G. C.; Diner, B. A. *Biochemistry* Submitted for publication.

(22) (a) Svensson, B.; Vass, I.; Cedergren, E.; Styring, S. *EMBO J.* **1990**, *9*, 2051−2059. (b) Ruffle, S. V.; Donnelly, D.; Blundell, T. L.; Nugent, J. *Photosynth. Res.* **1992**, *34*, 287−300.

(23) Svensson, B.; Vass, I.; Styring, S. *Z. Naturforsch.* **1991**, *46c*, 765−776.

(24) Bernard, M. T.; MacDonald, G. M.; Nguyen, A. P.; Debus, R. J.; Barry, B. A. *J. Biol. Chem.* **1995**, *270*, 1589−1594.

(25) (a) Stubbe, J. *Annu. Rev. Biochem.* **1989**, *58*, 257−285. (b) Barry, B. A. *Photochem. Photobiol.* **1993**, *57*, 179−188. (c) Hoganson, C. W.; Babcock, G. T. In *Metal Ions in Biological Systems;* Sigel, H., Sigel, A., Eds.; Marcel Dekker: New York, 1994; Vol. 30, pp 77−107. (d) Thelander, A.; Gräslund, A. In *Metal Ions in Biological Systems;* Sigel, H., Sigel, A., Eds.; Marcel Dekker: New York, 1994; Vol. 30, pp 109−129.

(26) Rippka, R.; Deruelles, J.; Waterbury, J. B.; Herdman, M.; Stainer, R. Y. *J. Gen. Microbiol.* **1979**, *111*, 1−61.

(27) Barry, A. B.; Babcock, G. T. *Proc. Natl. Acad. Sci. U.S.A.* **1987**, *84*, 7099−7103.

described in Tang and Diner.[28] The modifications[21] include breaking the cells in buffer A containing 50 mM HEPES−NaOH buffer, pH 7.2, instead of MES−NaOH, pH 6.0, and following the DEAE−Toyopearl ion exchange chromatography by a second column step on hydroxylapatite, according to Rögner *et al.*[29] The PSII core complexes are completely inactive for oxygen evolution as isolated and contain no EPR detectable Mn. The PSII-containing fractions were concentrated by using Centriprep 100 s (Amicon). The HPLC elution buffer was then exchanged with buffer A (50 mM MES−NaOH, pH 6.0, 25% glycerol (w/v), 5 mM $CaCl_2$ and 5 mM $MgCl_2$) in desalting columns (Bio-Rad. Econo-Pac 10 DG) and the core complexes were further concentrated by using Centricon 100 s (Amicon).

The samples were made 0.3 mM in $K_3Fe(CN)_6$ and placed in EPR tubes. $Y_Z^\bullet$ was trapped by freezing under illumination with white light provided by a 150-W lamp (Cuda Products Corp. Model I-150).[21] The samples were stored in liquid nitrogen until use to prevent loss of the trapped radical.

In the ^2H_2O-exchange experiments, the PSII core complexes were transferred to a buffer containing 20 mM HEPES−NaOH (pD 7.5) and 10 mM NaCl in ^2H_2O, followed by 15 h of incubation at 4 °C in the dark. A parallel experiment was performed in ^1H_2O (pH 7.5) under the same conditions. Following these incubations, the $Y_Z^\bullet$ radical was trapped as described above.

EPR and ENDOR Spectroscopies. EPR spectra were recorded by using a Bruker ER200D X-band spectrometer equipped with a TE102 mode cavity. For ENDOR measurements, the instrument was used in conjunction with a Bruker ER250 ENDOR accessory and a ER250ENB TM011 cavity. A Wavetek (Model 3000-446) radio frequency (rf) synthesizer and an ENI 3100L power amplifier were employed for conventional frequency-modulated ENDOR spectroscopy. The transient ENDOR apparatus was constructed at Michigan State University.[30] The design of the 18-turn ENDOR rf coil used has been described.[31] EPR and ENDOR spectra were recorded at liquid nitrogen temperatures by using a N_2 gas flow system supplied by Bruker. Measurements of microwave frequencies and magnetic field strengths were made by using a Hewlett-Packard 5355A frequency converter/5245L counter and a Bruker ER035 gaussmeter, respectively. Signal averaging of EPR and ENDOR spectra was performed in a personal computer interfaced with the spectrometer.

ESEEM Spectroscopy. The pulsed EPR spectrometer was locally built at Michigan State University.[32] The minimum dead time of the spectrometer was 120 ns. Dead-time reconstruction of the time domain data was performed as described.[33] The frequency-domain ESEEM spectra were obtained by calculating the Fourier transforms of the time-domain data. Computation of powder ESEEM spectra was performed by using the Matlab program supplied by The Mathworks Inc. (Natick, MA). The simulations were based on the theoretical formalism developed by Mims.[34] Dead-time reconstruction and Fourier transformations of the simulated time-domain spectra were performed in the same manner as for the experimental data.

Results

CW-EPR Spectroscopy. The top trace in Figure 1 displays the X-band continuous-wave EPR line shape of $Y_Z^\bullet$, generated and trapped as described in the Materials and Methods section in the Y_D-less, D2-Y160F, mutant of *Synechocystis* 6803. The $Y_Z^\bullet$ radical is immobilized in randomly oriented protein complexes and the resulting anisotropic interactions give rise to the partially resolved, powder-type spectrum shown in Figure

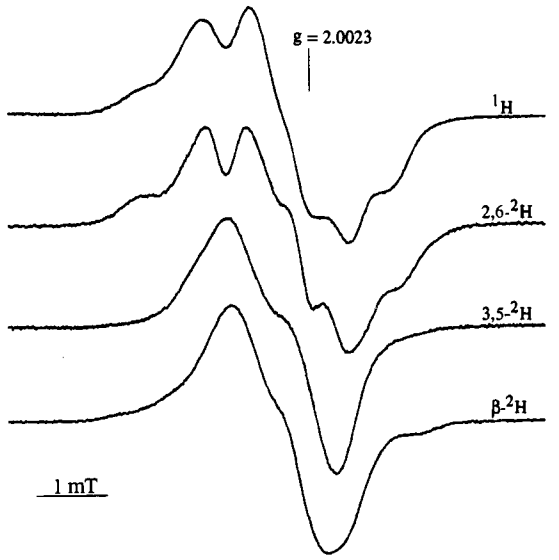

Figure 1. EPR spectra of $Y_Z^\bullet$ in the Mn-depleted PSII core complex of the D2-Y160F mutant strain created in the cyanobacterium *Synechocystis* 6803. The radical was induced in light and trapped at low temperature. The spectra represent the Y_Z radical from cells grown in normal medium or in the presence of specifically ^2H-labeled tyrosine as indicated. Experimental conditions: microwave frequency 9.547 GHz, microwave power 0.4 mW, modulation amplitude 0.25 mT; time constant 100 ms; scan rate 0.1 mT/s; temperature 115 K.

1. The spectrum exhibits a peak-to-trough line width of 2 mT and a g-value at the zero-crossing of 2.0045.

Also shown in Figure 1 are spectra of $Y_Z^\bullet$ from cells grown in the presence of tyrosine specifically labeled with deuterium at the ring 2,6- and 3,5-positions or the β-methylene position.[35] Because $\gamma(^1H) = 6.5\gamma(^2H)$, introducing deuterium will reduce the hyperfine splitting from the isotopically exchanged site by a factor of 1/6.5 and, thus, provide a means to obtain qualitative information on the individual hyperfine contributions to the EPR spectrum. The spectrum obtained after ^2H-labeling at the 2,6-positions is only slightly different from that of the fully protonated form of $Y_Z^\bullet$. In contrast, upon deuteration at the 3,5-position or at the β-methylene position, the hyperfine structure collapses and the overall line widths are, in both cases, reduced significantly.

The line shapes displayed in Figure 1 are similar to those reported for the ^2H-labeled Y_D radical.[36] This shows that the $Y_Z^\bullet$ spin-density distribution follows the same odd-alternate pattern, with high values at the O, C_1, C_3, and C_5 atoms and low values at the C_2, C_4, and C_6 carbons observed for $Y_D^\bullet$[10,11] and other protein-associated tyrosyl radicals.[10a,37,38] The results presented above are in agreement with earlier EPR studies on specifically ^2H-labeled $Y_Z^\bullet$.[20b]

The EPR spectra in Figure 1 provide qualitative, but not quantitative, information on $Y_Z^\bullet$ spin densities. To obtain a more detailed assessment of the spin-density distribution and information on the structure and hydrogen-bonding status of $Y_Z^\bullet$, the specifically ^2H-labeled samples were examined by using

(28) Tang, X.-S.; Diner, B. A. *Biochemistry* **1994**, *33*, 4594−4603.
(29) Rögner, M.; Nixon, P J.; Diner, B. A. *J. Biol. Chem.* **1990**, *265*, 6189−6196.
(30) Hoganson, C. W.; Babcock, G. T. *J. Magn. Reson., Ser. A* **1995**, *112*, 220−224.
(31) Bender, C. J.; Babcock, G. T. *Rev. Sci. Instrum.* **1992**, *63*, 3523−3524.
(32) McCracken, J. L.; Shin, D.-H.; Dye, J. L. *Appl. Magn. Reson.* **1992**, *3*, 305−316.
(33) Mims, W. B. *J. Magn. Reson.* **1984**, *59*, 291−306.
(34) (a) Mims, W. B. *Phys. Rev. B* **1972**, *5*, 2409−2419. (b) Mims, W. B. *Phys. Rev. B.* **1972**, *6*, 3543−3545.
(35) For numbering of the aromatic moiety of the tyrosine, see Figure 8.
(36) Barry, B. A.; El-Deeb, M. K.; Sandusky, P. O.; Babcock, G. T. *J. Biol. Chem.* **1990**, *265*, 20139−20143.
(37) Bender, C. J.; Sahlin, M.; Babcock, G. T.; Barry, B. A.; Chandrashekar, T. K.; Salowe, S. P.; Stubbe, J.; Lindström, B.; Petersson, L.; Ehrenberg, A.; Sjöberg, B.-M. *J. Am. Chem. Soc.* **1989**, *111*, 8076−8083.
(38) (a) Babcock, G. T.; El-Deeb, M. K.; Sandusky, P. O.; Whittaker, M. M.; Whittaker, J. W. *J. Am. Chem. Soc.* **1992**, *114*, 3727−3734.

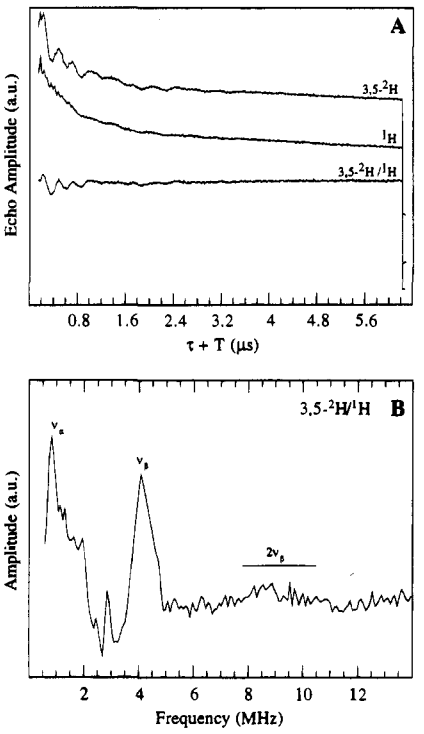

Figure 2. (A) Electron spin-echo envelopes obtained from the 3,5-^{2}H labeled and non-deuterated Y_Z radical along with the 3,5-^{2}H/^{1}H quotient spin-echo envelope. Each waveform represents the sum of several echo envelopes obtained at different τ-values. The τ-values were chosen so as to comprise a whole number of cycles of the ^{1}H Larmor period, in order to suppress contributions of ^{1}H-nuclei to the spectra, and are indicated within parentheses in the following. (B) Fourier transforms of the 3,5-^{2}H/^{1}H quotient summation spin-echo envelope. Experimental conditions: τ 176 (×3), 235 (×4), 293 (×5), 352 (×6), 469 (×8), 587 (×10), 704 (×12), 821 (×14), 939 (×16), 1056 ns (×18); (τ + T_0) 140 ns; microwave frequency 11.208 GHz; magnetic field 0.4004 T; microwave pulse power 40 W (20 ns fwhm); pulse sequence repetition rate 10 Hz; temperature 4 K; ν_{2H} = 2.6 MHz.

two high-resolution, electron magnetic-resonance techniques, ESEEM and ENDOR.

Hyperfine Coupling Tensors at the 3,5-Positions. The CW-EPR spectra of $Y_Z^\bullet$ show that the hyperfine couplings to the α-^{1}H at the 3,5-positions are substantial (Figure 1). The hyperfine tensors for these ring hydrogens are expected to be rhombic with principal values roughly in the ratio of 1:$^3/_2$:$^1/_2$.[39] These values correspond to the A_x, A_y, and A_z principal hyperfine components in an orthogonal axis system with x along the p_z orbital on the carbon and z along the C_α–H_α bond. For such strongly anisotropic hyperfine tensors, the ENDOR resonances are severely broadened and conventional application of this spectroscopy is at a disadvantage, particularly when the radical spin concentration is low, as it was for the $Y_Z^\bullet$ samples. Warncke and McCracken,[40] however, have shown recently that pulsed-EPR techniques can be used to determine ^{2}H-tensor components directly in specifically deuterated radicals. For ^{2}H substituted at α-positions, the anisotropic character of the hyperfine tensors, the reduction in spectral extent, the lower gyromagnetic ratio of ^{2}H relative to ^{1}H, and the I = 1 property of the ^{2}H nucleus all favor application of the ESEEM technique, and we have used it here to characterize the 3,5-positions in $Y_Z^\bullet$.

^{2}H-ESEEM Spectroscopy. The top and middle traces in Figure 2A display respectively stimulated electron spin-echo envelope modulation patterns collected from the 3,5-^{2}H labeled and the fully protonated Y_Z radical at a magnetic field of 0.4004 T. The time-domain spectra were obtained by using a 3-pulse, 90°–τ–90°–T–90°, microwave pulse sequence with pulse-swapping.[40,41] In a typical 3-pulse experiment, τ, the time between pulses I and II, is held constant while T, the time between pulses II and III, is varied. A plot of echo amplitude vs T then traces out the spin-echo envelope modulation patterns in the upper two traces. The modulations observed in the spin-echo envelopes arise from the hyperfine interactions between the unpaired electron spin and magnetic nuclei in its environment. As observed in the upper trace in Figure 2A, the hyperfine couplings to the ^{2}H-nuclei give rise to strong modulation of the echo envelope. The bottom trace represents the quotient envelope obtained by dividing the 3,5-^{2}H echo envelope by that from the fully protonated sample. Division of the time-domain data was performed to emphasize the contributions from the ^{2}H-nuclei and to reduce spectral modulations common to both samples.[42] The pulse-swapping and waveform-division techniques have been used previously for a detailed characterization of specifically ^{2}H-labeled samples of the Y_D radical in PSII.[11]

In 3-pulse stimulated ESEEM spectra, the intensities of the ν_α and ν_β hyperfine frequencies, associated with the $+^1/_2$ and $-^1/_2$ electron spin manifolds, respectively, are correlated.[34] The amplitude of the hyperfine frequency ν_α is modulated by a [1 − cos($2\pi\nu_\beta\tau$)] term; similarly, the ν_β peak is dependent on a [1 − cos($2\pi\nu_\alpha\tau$)] term. In addition to this τ-dependent suppression effect, the position and shape of the individual ESEEM lines are sensitive to the microwave frequency and the external magnetic-field strength.[43]

A systematic investigation of the 3,5-^{2}H hyperfine couplings was performed. The 3,5-^{2}H and fully protonated $Y_Z^\bullet$ species were investigated at two different microwave frequencies, 9.190 (zero-crossing field H_0 = 0.3278 T) and 11.208 GHz (H_0 = 0.4004 T). At each field, a set of ESEEM spectra was generated as a function of τ. All τ-values were chosen so as to comprise whole cycles of the ^{1}H Larmor period to suppress the modulations from matrix ^{1}H nuclei.[34b,42]

The 3,5-^{2}H and ^{1}H spin-echo envelopes shown in Figure 2A were obtained by summing time-domain data recorded at different τ-values. Figure 2B shows the Fourier transform of the summed 3,5-^{2}H/^{1}H quotient spin-echo envelope displayed in Figure 2A. Owing to the summation procedure, the line shape represents the 3,5-^{2}H hyperfine transitions where the influence of the τ-dependent suppression effect is minimized. Consequently, the summation line shape shows more clearly the full complement of 3,5-^{2}H hyperfine frequencies compared to the individual spectra, which are influenced by τ-suppression.[40] The frequency spectrum exhibits two regions of high spectral intensity positioned symmetrically about the deuterium Larmor frequency (ν_{2H} = 2.6 MHz at 0.4004 T). The feature centered at 4.2 MHz represents the fundamental ν_β hyperfine frequency components that correspond to the $\Delta m_I = \pm 1$ transitions within the $-^1/_2$ electron spin manifold. The corresponding ν_α peak is found on the low-frequency side of ν_{2H} and is centered around 1.2 MHz. However, in this region, the spectral line shape is

(39) McConnell, H. M.; Heller, C.; Cole, T.; Fessenden, R. W. *J. Am. Chem. Soc.* **1960**, *82*, 766–775.
(40) Warncke, K.; McCracken J. *J. Chem. Phys.* **1994**, *101*, 1832–1841.
(41) (a) Fauth, J.-M.; Schweiger, A.; Braunschweiler, L.; Forrer, J.; Ernst, R. R. *J. Magn. Reson.* **1986**, *66*, 74–85. (b) Fauth, J.-M.; Schweiger, A.; Ernst, R. R. *J. Magn. Reson.* **1989**, *81*, 262–274.
(42) Mims, W. B.; Peisach, J. In *Advanced EPR: Applications in Biology and Biochemistry;* Hoff, A. J., Ed.; Elsevier: New York, 1989; pp 1–57.
(43) Singel, D. J. In *Advanced EPR: Applications in Biology and Biochemistry*; Hoff, A. J., Ed.; Elsevier: New York, 1989; pp 119–133.

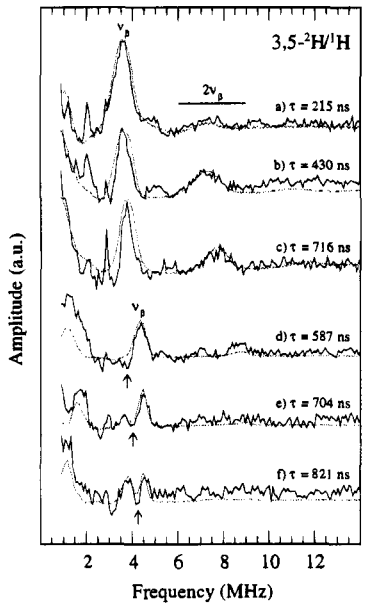

Figure 3. Fourier transforms of 3,5-^{2}H/^{1}H quotient electron spin-echo envelopes obtained at two different microwave frequencies and using different τ-values. The τ-values used to generate each spectrum in units of $1/\nu_{1H}$ are indicated within parentheses. Simulated spectra (dotted lines) overlay the corresponding experimental spectra (solid lines). The calculated spectra are generated with the hyperfine parameters given in Table 1. Experimental conditions: (a−c) microwave frequency 9.190 GHz; magnetic field 0.3278 T; τ 215 (×3), 430 (×6), 716 (×10) ns; $(\tau + T_0)$ 140 ns; $\nu_{2H} = 2.1$ MHz; (d−f) microwave frequency 11.208 GHz; magnetic field strength 0.4004 T; τ 587 (×10), 704 (×12), 821 (×14) ns; $(\tau + T_0)$ 140 ns; $\nu_{2H} = 2.6$ MHz; (a−f) microwave pulse power 40 W (20 ns fwhm); pulse sequence repetition rate 10 Hz; temperature 4 K.

complicated by the appearance of peaks not associated with the ^{2}H hyperfine transitions.[44] A broad feature, centered around 9 MHz and corresponding to the $2\nu_\beta$, double-quantum ($\Delta m_I = \pm 2$) ^{2}H transitions, is also observed in the spectrum.

Figure 3 displays individual 3,5-^{2}H/^{1}H quotient frequency-domain spectra obtained at single τ-values at either 0.3278 (Figure 3a−c) or 0.4004 T (3d−f). The τ-values used to generate the spectra were chosen in units of $1/\nu_{1H}$, i.e., as multiples of the Larmor period of the ^{1}H nucleus at the magnetic field used. Spectra c and d, which were obtained at τ-values that correspond to 10 times $1/\nu_{1H}$ at their respective magnetic fields, show the dependence of the ESEEM lines on the external magnetic-field intensity. In the spectrum obtained at 0.3278 T (Figure 3c), the maximum of the fundamental ν_β peak is centered at 3.8 MHz, while in the spectrum obtained at 0.4004 T (Figure 3d), the peak is shifted to a position of 4.3 MHz. Thus, this resonance moves in concert with the deuterium Larmor frequency, which is 2.1 MHz at 0.3278 T and 2.6 MHz at 0.4004 T, and confirms its ^{2}H origin. The spectral features representing the $2\nu_\beta$ hyperfine frequencies shift about twice as much at the two different fields, from 7.8 to 8.8 MHz, as expected. The three bottom spectra, obtained at 0.4004 T, show the τ-dependent suppression effect on the ESEEM line shape. The amplitude of the ν_β fundamental peak, positioned at 4.3 MHz, is low and

(44) Additional features are seen in the spectra in Figures 2B and 7B at 0.8, 1.5, 2.5, and 2.8 MHz. These are most likely ^{14}N resonance from a chlorophyll radical present at low concentration. They were absent in ESEEM spectra recorded in the wings of the $Y_Z^\bullet$ EPR spectrum, whereas the ^{2}H resonance assigned to $Y_Z^\bullet$ persisted at these fields (not shown). Moreover, we found that the intensities of the contaminating peaks varied from sample to sample. Because of the strong ESEEM intensities of ^{14}N resonances, minor contaminating chlorophyll radical concentrations (5% of $Y_Z^\bullet$) will be apparent in the ESEEM spectra.

Table 1. Principal Hyperfine Tensor Components for the Y_z Tyrosyl Radical in Photosystem II

ENDOR transition	ENDOR freq[a,b]	assignment[c]	hyperfine coupling[a]	figure no.
a′,a	12.7; 16.0	β-$H_W \sim A_{iso}$	3.3 (0.5 ^{2}H)	4
		β-$H_W A_x$	1.7 (0.3 ^{2}H)	7
		β-$H_W A_y$	1.0 (0.15 ^{2}H)	7
		β-$H_W A_z$	7.9 (1.2 ^{2}H)	7
		2,6 A_x	1.3 (0.2 ^{2}H)	5
b′,b	11.8; 16.8	2,6 A_y	5.0 (0.8 ^{2}H)	4, 5
c′,c	10.5; 18.0	2,6 A_z	7.5 (1.1 ^{2}H)	4, 5
d	24.0	3,5 A_x	−19.5 (−3.0 ^{2}H)	2, 3, 6
		3,5 A_y	−26.8 (−4.1 ^{2}H)	2, 3
		3,5 A_z	−8.4 (−1.3 ^{2}H)	2, 3
e	29.4	β-$H_S \sim A_{iso}$	30.2 (4.6 ^{2}H)	6
		β-$H_S A_x$	29.2 (4.5 ^{2}H)	7
		β-$H_S A_y$	28.5 (4.4 ^{2}H)	7
		β-$H_S A_z$	35.4 (5.4 ^{2}H)	7

[a] Given in units of MHz with an estimated error in measurement of ±0.1 MHz. [b] The ENDOR hyperfine frequencies were derived assuming an isotropic **g**-tensor. [c] β-H_s and β-H_w stand for the strongly and weakly coupled β-methylene ^{1}H (^{2}H), respectively.

the overall line shape is distorted by the suppression produced by the ν_α conjugate frequencies at the τ-values used. The upturned arrows in Figure 3 follow the spectral suppression effect created by the $[1 - \cos(2\pi\nu_\alpha\tau)]$ term, which tracks across the line shape of the ν_β peak as the τ-value increases.

The positions, the relative amplitudes, and the line shapes of the peaks corresponding to the fundamental- and double-quantum hyperfine frequencies in the ESEEM spectra as a function of τ, microwave frequency, and magnetic field provide constraints that allow complete determination of the 3,5 hyperfine coupling tensors by spectral simulation. Representative simulated spectra (dotted lines) are overlaid on the corresponding experimental spectra (solid lines) in Figure 3. The hyperfine couplings used to generate the simulated spectra are $A_x = -3.0$ MHz (−19.5 MHz ^{1}H), $A_y = -4.1$ MHz (−26.8 MHz ^{1}H), and $A_z = -1.3$ MHz (−8.4 MHz ^{1}H). These values are in agreement with ENDOR data reported below. The principal values result in an A_{iso} of −2.8 MHz (−18.2 MHz ^{1}H) for the 3,5-tensors. The hyperfine couplings are listed in Table 1. These values are comparable with those obtained from previous studies on biologically occurring tyrosyl radicals, which have shown that the magnitudes of the hyperfine couplings to the 3,5-^{1}H are on the order of 8, 20, and 26 MHz (±1 MHz)[10,11,37]

Hyperfine Coupling Tensors at the 2,6-Positions. Deuterium labeling at the α-2,6-positions gave detectable but minor effects on the EPR spectrum of $Y_Z^\bullet$ (Figure 1), indicating that the hyperfine couplings with the 2,6-hydrogens are relatively weak. By analogy to the α-3,5 hyperfine coupling tensors, the 2,6 coupling tensors are expected to be of rhombic symmetry.

CW-ENDOR Spectroscopy. The top spectrum in Figure 4 shows the continuous-wave ENDOR spectrum of fully protonated $Y_Z^\bullet$ in the 10−20 MHz frequency range. The powder spectrum exhibits a large unresolved line centered at the Larmor frequency of the ^{1}H nucleus (14.3 MHz), which represents the combined contribution from weakly coupled hydrogens in the vicinity of the radical. In addition to the matrix line, three sets of peaks, labeled a−c, are observed in the spectrum. Two of these, positioned at 10.5 and 18.0 MHz (c′,c) and at 11.8 and 16.8 MHz (b′,b), have the characteristic line shapes of rhombic tensor components (e.g. 45). On the basis of the overall magnitude of the couplings and the line shapes observed, these peaks are assigned to the 2,6-tensors with the ν_β transitions at the low-frequency side and the ν_α transitions at the high-frequency side of the ^{1}H Larmor frequency. Due to the low-spin concentration in the 2,6-^{2}H labeled sample (<10 μM),

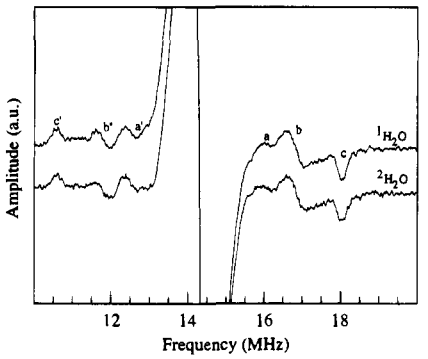

Figure 4. Continuous-wave ENDOR spectra of $Y_Z^\bullet$ in PSII core complexes incubated in ^1H_2O buffer or ^2H_2O buffer. Each spectrum was obtained at the zero-crossing of the corresponding EPR spectrum. The labeled ENDOR transitions are listed in Table 1. Experimental conditions: microwave frequency 9.399 GHz; magnetic field 0.3350 T; microwave power 2.0 mW; radio frequency power 120 W (at 15 MHz); FM amplitude 100 kHz; time constant 500 ms; scan rate 50 kHz/s; temperature 114 K; $\nu_{^1H} = 14.3$ MHz.

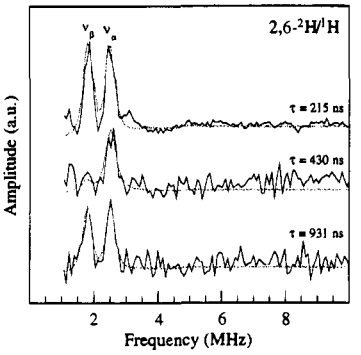

Figure 5. Fourier transforms of 2,6-$^2H/^1H$ quotient electron spin-echo envelopes. A conventional ($T > 0$) 3-pulse microwave sequence was used for $\tau = 215$ ns and the pulse-swapping sequence for τ-values of 430 and 931 ns. The τ-values are given in units of $1/\nu_{^1H}$ within parentheses. Simulated spectra (dotted lines) overlay the corresponding experimental spectra (solid lines). The simulated spectra were generated with the hyperfine parameters given in Table 1. Experimental conditions: microwave frequency 9.190 GHz; magnetic field strength 0.3278 T; τ 215 (×3), 430 (×6), 931 (×13) ns; ($\tau + T_0$) 140 ns; microwave pulse power 40 W (20 ns fwhm); pulse sequence repetition rate 10 Hz; temperature 4 K; $\nu_{^2H} = 2.1$ MHz

ENDOR spectra could not be obtained to allow an unambiguous assignment. This problem could be circumvented by collecting complementary ^2H-ESEEM spectra.

^2H-ESEEM Spectroscopy. The third and smallest of the 2,6-tensor components, A_x, was not observed in the ENDOR spectrum since it was obscured by the large matrix feature (Figure 4). However, the A_x component could successfully be determined by using the ^2H-ESEEM technique. Figure 5 shows 2,6-$^2H/^1H$ quotient ESEEM frequency-domain spectra of $Y_Z^\bullet$. The spectra were collected at a magnetic field strength of 0.3278 T at three different values of τ. At τ equal 215 or 931 ns, two peaks, symmetrically positioned about the Larmor frequency of the ^2H nucleus and split by 0.7 MHz (4.6 MHz ^1H), are clearly seen. These two peaks, centered at 1.8 and 2.5 MHz, represent the ν_β and ν_α hyperfine frequencies of the 2,6-sites, respectively. In the spectrum recorded with τ set to 430 ns, which is close to $1/\nu_\alpha$, the τ-dependent suppression effect is clearly manifested as the peak that arises from the ν_β manifold is eliminated.

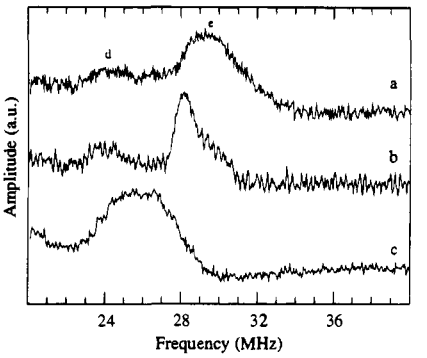

Figure 6. Transient-detected ENDOR spectra representing (a) the Y_Z radical in *Synechocystis*, (b) the Y_D radical in spinach, and (c) the Y_D radical in *Synechocystis*. Each ENDOR spectrum was obtained at the zero-crossing of the corresponding EPR spectrum and are displayed in absorption mode. The labeled hyperfine transitions are listed in Table 1. Experimental conditions: microwave frequency 9.399 GHz; magnetic field strength 0.3351 T; microwave power 2.0 mW, step size 50 kHz; off-resonance baseline subtractions were performed; temperature 108 K; $\nu_{^1H} = 14.3$ MHz.

Simulated spectra (dotted lines) are shown together with the experimental spectra (solid lines) in Figure 5. They were calculated by using the experimental settings, a hyperfine value of $A_x = 0.2$ MHz (1.3 MHz ^1H), and the components derived from the ENDOR spectrum (Figure 4), $A_y = 0.8$ MHz (5.0 MHz ^1H) and $A_z = 1.1$ MHz (7.5 MHz ^1H). The magnitude of the principal components results in an A_{iso} of 0.7 MHz (4.6 MHz ^1H). The close agreement between the experimental and calculated spectra verifies the combined ENDOR/ESEEM assignments of the tensor components (Table 1).

Hyperfine Coupling Tensors at the β-Methylene Position. The effects on the EPR spectrum of $Y_Z^\bullet$ upon specific ^2H-labeling show that, in addition to the 3,5-^1H, there is a strong hyperfine contribution that involves the hydrogens covalently bound to the β-methylene carbon (Figure 1). This is consistent with previous studies on $Y_D^\bullet$, which showed that one of the two β-^1H had a substantial hyperfine coupling to the unpaired electron spin density.[10,11] For these β-^1H, the hyperfine interactions are more isotropic.[46] This favors detection by ENDOR since the narrow and more intense features of β-^1H contribute much more strongly to the spectrum than do the anisotropically broadened features of α-^1H.

Transient-Detected ENDOR Spectroscopy. The spin concentrations of the fully protonated $Y_Z^\bullet$ samples were too low (<20 μM) to allow detection by CW-ENDOR of resonances in the higher-frequency (≥20 MHz) region. However, a transient-detected ENDOR technique[30] provides increased sensitivity, as compared to the conventional steady-state method, and was successfully employed. The top trace in Figure 6 shows the transient ENDOR spectrum of $Y_Z^\bullet$ between 20 and 40 MHz.[47] The transient EPR response is plotted as a function of the radio frequency applied, which provides an absorption ENDOR spectrum. The broad resonance in the 20-28 MHz region represents the rhombic hyperfine coupling tensors of the 3,5-^1H in agreement with the ESEEM data presented above (Table 1). In addition, a feature spanning from 28 to 35 MHz with a maximum at 29.4 MHz is apparent in the spectrum. This peak is assigned to the strongly coupled β-methylene hydrogen, β-^1H_S, of the Y_Z radical.

(45) (a) Gordy, W. In *Techniques of Chemistry, Volyme XV: Theory and Applications of Electron Spin Resonance;* West, W., Ed.; John Wiley & Sons, Inc.: New York, **1980**. (b) Weil, J. A.; Wertz, J. E.; Bolton, J. R. *Electron Spin Resonance: Elementary Theory and Practical Applications;* John Wiley & Sons, Inc.: New York, 1994.

(46) Heller, C.; McConnell, H. M. *J. Chem. Phys.* **1960**, *32*, 1535–1539.

Also shown in Figure 6 are transient ENDOR spectra for $Y_D^\bullet$ from spinach (Figure 6b) and from *Synechocystis* (Figure 6c). In agreement with earlier work,[10] the couplings in the 20−28 MHz region for $Y_D^\bullet$ in spinach are assigned to 3,5-^{1}H; the β-^1H_S resonances occur in the 27.5−31 MHz range and are significantly sharper and narrower than the $Y_Z^\bullet$ β-^1H_S resonances in Figure 6a (see below). In the *Synechocystis* $Y_D^\bullet$ spectrum (Figure 6c), the β-^1H_S coupling overlaps the 3,5-^{1}H resonances in the 24.5−28 MHz range, consistent with earlier ENDOR[10a] and ESEEM[11] studies on this species. The differences in β-^1H_S couplings in *Synechocystis* $Y_Z^\bullet$ (Figure 6a) and $Y_D^\bullet$ (Figure 6c) support the conclusion that the EPR spectral line shapes of these two radicals are slightly different and provide a basis to understand the differences.[20,21]

CW-ENDOR Spectroscopy. The hyperfine coupling tensors of the β-methylene position are expected to be strongly inequivalent with the more weakly coupled ^{1}H (^{2}H) fairly close to the Larmor frequency of the coupled nucleus. The only ENDOR peaks left to account for are the hyperfine transitions labeled a',a in Figure 4, positioned at 12.7 and 16.0 MHz. These features are assigned to the hyperfine interactions of the weakly coupled β-methylene hydrogen, β-^1H_W, of $Y_Z^\bullet$. As was the situation with respect to the 2,6 hyperfine coupling tensors, the spin concentrations of the 3,5-^{2}H and β-^{2}H labeled samples were too low to allow ENDOR measurements, which prevented an unambiguous assignment of the hyperfine components of the β-^{1}H from the ENDOR spectroscopy alone. However, ESEEM spectra from the β-^{2}H labeled sample could be obtained. These data support a β-^{1}H origin of the ENDOR resonances observed in Figures 4 and 6a and allowed determination of the principal hyperfine components.

^{2}H-ESEEM Spectroscopy. Figure 7A displays frequency-domain spectra of β-^{2}H/^{1}H quotient spin-echo envelopes. Each spectrum was obtained by adding ten sets of time-domain data, collected at different τ-values, followed by Fourier transform of the summation envelopes. The frequency-domain spectrum obtained at a center field of 0.3278 T (top trace) shows a peak at 4.5 MHz and a broad feature centered at 9 MHz. These features move in concert with the Larmor frequency of the ^{2}H nucleus, as shown in the spectrum obtained at a center field of 0.4004 T (bottom trace), which confirms that they are associated with deuterium hyperfine transitions. These two features are assigned to the ν_α and $2\nu_\alpha$ hyperfine frequencies of the strongly coupled β-^2H_S, respectively. The position of the β-^2H_S ν_α peak in the ESEEM spectrum corresponds to the β-^1H_S ENDOR features in Figure 6a. Furthermore, the β-^1H_W assignment of the hyperfine transitions observed at 12.7 and 16.0 MHz in Figure 4 is supported by the ESEEM spectra. A close examination of the congested region around the deuterium Larmor frequency in the two spectra indicates that there are peaks moving in accordance with ν_{2H} at the two magnetic fields.[44]

Analysis of the ESEEM spectra was performed to extract the principal values of the β-^{2}H hyperfine coupling tensors. However, in contrast to the 2,6-^{2}H and 3,5-^{2}H ESEEM features (Figures 3 and 5), the relatively broad line shape of the fundamental β-^2H_S hyperfine transitions could not be reproduced by ESEEM simulations that incorporated discrete hyperfine tensors and a C_1 spin density consistent with our conclusion about ρ-values at the other ring positions (see Discussion). Specifically, ϱ_{C_1} values ≥ 0.8 were needed to simulate the line width and amplitude of the β-^2H_S ν_α feature when only a single hyperfine interaction was considered.

A discrete hyperfine tensor has also been found inappropriate for the description of ESEEM from β-^{2}H hyperfine coupling in model tyrosyl radicals trapped in low-temperature aqueous glass.[48] In the model radical, a "frozen in" distribution of the

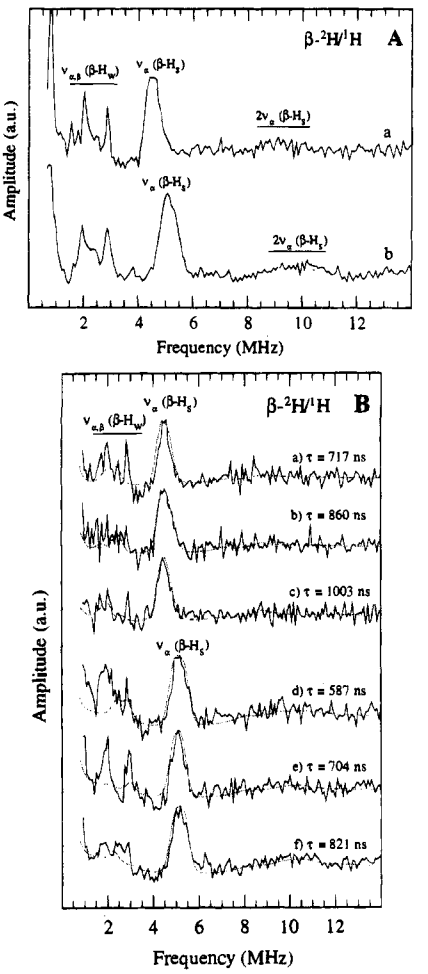

Figure 7. (A) Fourier transforms of β-methylene ^{2}H/^{1}H quotient summation spin-echo envelopes obtained at two different microwave frequencies. The τ-values used comprise integer number of the ^{1}H Larmor period and are indicated within parentheses in the following. Experimental conditions: (a) microwave frequency 9.190 GHz; magnetic field 0.3278 T; τ 215 (×3), 287 (×4), 358 (×5), 430 (×6), 573 (×8), 716 (×10), 860 (×12), 1003 (×14), 1146 (×16), 1290 ns (×18); ($\tau + T_0$) 140 ns; ν_{2H} = 2.1 MHz; (b) microwave frequency 11.208 GHz; magnetic field 0.4004 T; τ 176 (×3), 235 (×4), 293 (×5), 352 (×6), 469 (×8), 587 (×10), 704 (×12), 821 (×14), 939 (×16), 1056 ns (×18); ($\tau + T_0$) 140 ns; ν_{2H} = 2.6 MHz; (a−b) microwave pulse power 40 W (20 ns fwhm); pulse sequence repetition rate 10 Hz; temperature 4 K. (B) Fourier transforms of individual β-methylene ^{2}H/^{1}H quotient echo envelopes. Simulated spectra (dotted lines) overlay the corresponding experimental spectra (solid lines). ESEEM simulations of the distributed β-^{2}H interactions were performed as described.[48] The simulated spectra incorporate contributions from different C_1−C_β rotamers, in increments of 2°, as follows: θ = 48°, 46°, 44°, 42°, 40°, 38°, 36° (β-^2H_S) and 72°, 74°, 76°, 78°, 80°, 82°, 84° (β-^2H_W). Experimental conditions: (a−c) microwave frequency 9.190 GHz; magnetic field strength 0.3278 T; τ 717 (×10), 860 (×12), and 1003 (×14) ns; ($\tau + T_0$) 140 ns; ν_{2H} = 2.1 MHz; (d−f) microwave frequency 11.208 GHz; magnetic field 0.4004 T; τ 587 (×10), 704 (×12), and 821 (×14) ns; ($\tau + T_0$) 140 ns; ν_{2H} = 2.6 MHz; (a−f) microwave pulse power 40 W (20 ns fwhm); pulse sequence repetition rate 10 Hz; temperature 4 K.

(47) The transient spectrum of $Y_Z^\bullet$ in Figure 6 was obtained at 108 K, rather than at lower temperatures, since the relaxation mechanisms of the Y_Z radical in the Mn-depleted particles at liquid helium temperatures were sufficiently slow that the spin system could not track the applied field as the system was swept through resonance. Even with a field modulation of 12.5 kHz, the EPR line shape of $Y_Z^\bullet$ was severely distorted at these temperatures, indicating that the system was in adiabatic rapid passage (not shown).

orientation of the phenoxyl ring with respect to the β-^{2}H is found that is caused by rotational mobility about the C_1-C_β bond[49] prior to freezing.[48] The range of conformations around the C_1-C_β bond causes a spread in the ESEEM resonance frequencies of the β-^{2}H and, as a result, broadens the ESEEM line shapes. The ESEEM methods for analyzing distributed ^{2}H hyperfine interactions have been described.[48] Figure 7B displays experimental and simulated spectra obtained at different τ-values and resonant magnetic fields. The ESEEM simulations incorporate sets of C_1-C_β rotamers corresponding to values of θ for the strongly and weakly coupled β-^{2}H nuclei of 48°−36° and 72°−84°, respectively. The simulated line shapes match well the experimental line shapes of the strongly coupled β-^2H_S, and, despite interference from the ^{14}N lines of contaminating chlorophyll radicals,[44] are consistent with the observed intensity of the weakly coupled β-^2H_w in the spectral region near ν_N for ^{2}H.

Hyperfine Couplings to ^2H_2O Exchangeable Hydrogens. Hydrogen-bonding interactions have been observed in solid-state ENDOR and are characterized by purely dipolar coupling tensors of axial symmetry (e.g. 50). To investigate the hydrogen-bonding status of $Y_Z^\bullet$, ENDOR spectra were recorded from PSII core complexes incubated in ^1H_2O and ^2H_2O buffer for 15 h (Figure 4; top and bottom spectrum, respectively). The solvent isotope-exchange procedure allows identification of hyperfine couplings from exchangeable hydrogens in the vicinity of the tyrosyl radical. Other than a narrowing of the matrix line, which may reflect removal of weak couplings to distant, exchangeable hydrogens, or an alteration in $Y_Z^\bullet$ relaxation properties in ^2H_2O, no change in the $Y_Z^\bullet$ ENDOR coupling pattern in Figure 4 is observed for the radical in ^2H_2O relative to its spectrum in ^1H_2O. Spectra obtained with a lower FM modulation depth, and thus with higher resolution, gave the same result (not shown). We conclude that no well-ordered hydrogen bond, analogous to that observed for $Y_D^\bullet$,[12,13] can be observed for the Y_Z radical. Our observations do not eliminate, however, the possiblity that hydrogen bonds of varying strengths and distances occur in the $Y_Z^\bullet$ sites in our samples. Such disordered hydrogen bonding could broaden solvent isotope exchange-sensitive ENDOR resonances sufficiently to preclude their detection by CW-ENDOR techniques. We consider the alternative explanation, i.e., that $Y_Z^\bullet$ is inaccessible to solvent on the hours time scale, to be unlikely. $Y_Z^\bullet$ is considerably more accessible to reductant in the solvent phase than $Y_D^\bullet$,[51] consistent with the isotope-exchange effects observed in the matrix region in the spectra in Figure 4 (see also ref 21).

Discussion

Y_Z has been identified as Y161 of the D1 polypeptide and has been shown to play the functionally critical role of interfacing the photochemistry that occurs at the reaction center chlorophyll complex, P_{680}, in Photosystem II to the water-splitting chemistry that involves the $(Mn)_4$ cluster. Although the radical can be detected at room temperature by time-resolved techniques in O_2-evolving preparations and accumulated to concentrations approaching one per PSII center upon removal of the $(Mn)_4$ center, trapping the radical for detailed, low-temperature spectroscopic characterization has been problematic. Kawamori and her co-workers have had some success in achieving this recently in PSII preparations from higher plants.[14,20a] A difficulty with this approach is that the second redox-active tyrosine in PSII, $Y_D^\bullet$, occurs simultaneously in these preparations and complicates the spectral interpretation of $Y_Z^\bullet$. A second difficulty is that isotopic substitution methods have not been implemented in higher plant systems, which precludes spectral assignment based on isotope replacement.

The material developed for the study here avoids both of these difficulties and takes advantage of the demonstration by Tang *et al.*[21] that $Y_Z^\bullet$ can be trapped by freezing Mn-depleted cyanobacterial core complexes with illumination. By using cyanobacterial preparations in which Y_D has been genetically deleted, the spectral interpretation is simplified and can be done without relying on light−dark subtraction methods. Moreover, in *Synechocystis*, tyrosine auxotrophy can be implemented,[27] which has allowed us to base our spectral assignments on both protonated and specifically deuterated material. By using a combination of electron magnetic-resonance techniques and specific ^{2}H labeling, the principal components of the hyperfine tensors of six ^{1}H nuclei with significant hyperfine couplings in the Y_Z radical have been determined (Table 1). The magnitude and symmetry of these tensors provide information on the electronic and nuclear structure of $Y_Z^\bullet$. For the immobilized radical, the principal values of the hyperfine tensors reflect both isotropic and dipolar contributions; $A = A_{iso} + A_{dip}$. The magnitudes of the diagonal components are determined by the spatial distribution of the electron spin and the distances between the magnetic nuclei and the atoms that carry unpaired electron spin (e.g. 45,52). In the sections that follow, we analyze these tensors to extract structural and dynamic information on the Y_Z radical. We conclude by relating our spectroscopic work to functional aspects of water oxidation.

Spin-Density Distribution and Hydrogen Bonding in $Y_Z^\bullet$. The isotropic coupling for an α-H hyperfine tensor, whose magnitude is given by $A_{iso} = {}^1/_3\ \mathrm{Tr}\{A\}$, is due to a spin polarization mechanism and is proportional to the unpaired electron spin density, ρ, residing at the adjacent ring carbon:[53]

$$A_{iso} = \varrho Q \qquad (1)$$

where Q has been determined to be −69.6 MHz (^{1}H) for tyrosyl radicals.[37] By using the isotropic hyperfine couplings of −18.2 and 4.6 MHz for the hydrogens bound to the 3,5- and 2,6-positions, respectively (Table 1), and the McConnell relation above (eq 1), spin densities of 0.26 at C_3 and C_5 and −0.07 at C_2 and C_6 are obtained. We note that the A_{iso} values for the ortho and meta positions are consistent with the empirical relationship, $|A_{iso}(3,5\text{-}^1H) + A_{iso}(2,6\text{-}^1H)| = 13.2 \pm 0.6$ MHz, derived for a series of phenoxyl radicals by Dixon *et al.*[54]

The isotropic part of a β-methylene coupling tensor is due predominantly to hyperconjugation between the aromatic π-system of the ring and the 1s orbital on the β-H and is described by $A_{iso} = \rho_{C_1}(B_0 + B_2 \cos^2\theta)$[46] where θ is the dihedral angle defined by the $C_\beta-H_\beta$ bond and the axis of the p_z orbital on C_1, and B_2 is a constant equal to 162 MHz (^{1}H).[55] The B_0 term

(48) Warncke, K.; McCracken, J. *J. Chem. Phys.* In press.
(49) Sealy, R. C.; Harman, L.; West, P. R.; Mason, R. P. *J. Am. Chem. Soc.* **1985**, *107*, 3401−3411.
(50) (a) O'Malley, P. J.; Babcock, G. T. *J. Am. Chem. Soc.* **1986**, *108*, 3995−4001. (b) Fan, C.; Teixeira, M.; Moura, J.; Huynh, B.-H.; LeGall, J.; Peck, H. D., Jr.; Hoffman, B. M. *J. Am. Chem. Soc.* **1991**, *113*, 20−24.
(51) Yerkes, C. T.; Babcock, G. T.; Crofts, A. R. *FEBS Lett.* **1983**, *158*, 359−363.
(52) (a) Atherton, N. M. *Principles of Electron Spin Resonance;* Ellis Horwood and PTR Prentice Hall: London, 1993. (b) Piekara-Sady, L.; Kispert, L. D. In *Handbook of Electron Spin Resonance: Data Sources, Computer Technology, Relaxation, and ENDOR;* Poole, C. P., Jr., Farach, H. A., Eds.; AIP Press: New York, **1994**; pp 311−357.
(53) (a) McConnell, H. M. *J. Chem. Phys.* **1956**, *24*, 764−766. (b) McConnell, H. M.; Chesnut, D. B. *J. Chem. Phys.* **1958**, *28*, 107−117.
(54) Dixon, W. T.; Moghimi, M.; Murphy, D. *J. Chem. Soc., Faraday Trans. 2* **1974**, 1713−1720.
(55) Fessenden, R. W.; Schuler, R. H. *J. Chem. Phys.* **1963**, *9*, 2147−2195.

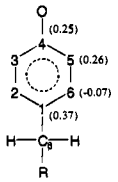

Figure 8. Spin-density distribution of the Y_Z radical in PSII.

includes the small nonhyperconjugative contributions and can be neglected,[11] which provides the simplified expression

$$A_{iso} = \varrho_{C_1} B_2 \cos^2\theta \qquad (2)$$

The analysis of the ESEEM data above for the β-methylene hydrogens in $Y_Z^\bullet$ shows that they are rotationally disordered in the protein environment. Within a rotationally distributed model, the spectra could be fit satisfactorily by using a C_1 spin density of 0.37 ± 0.03 and a spread in θ of ~14°. The most probable value of $A_{iso}(^1H)$ for the strongly coupled β-^1H_S in this analysis is 31.0 MHz, whereas that for the weakly coupled β-^1H_W is 3.5 MHz. The ESEEM data and analysis correlate well with the ENDOR data in Figures 4 and 6, as discussed below. From the densities for the ortho, meta, and para positions of the phenoxyl ring, we assign a total spin density of 0.25 to the C_4−O position. Figure 8 shows the overall spin-density distribution for the $Y_Z^\bullet$ radical.

The hydrogen-bond status of $Y_Z^\bullet$ differs significantly from that of $Y_D^\bullet$. For $Y_Z^\bullet$ we have not detected solvent-exchangeable features characteristic of well-ordered hydrogen bonds in its CW-ENDOR spectra. Tang *et al.*,[21] however, have found evidence from triple-resonance techniques for fairly strongly coupled, but broad, solvent-exchangeable features that they interpreted as a disordered hydrogen bond in $Y_Z^\bullet$. This is in contrast to the stable Y_D radical where ^2H_2O exchangeable features have been detected in ENDOR and ESEEM spectra of $Y_D^\bullet$ in spinach[12] and with ENDOR in *Synechocystis*[13] that indicate a specific, well-ordered hydrogen bond. The differences in hydrogen-bonding interactions for $Y_D^\bullet$ and $Y_Z^\bullet$ detected by magnetic resonance are reflected in recent site-directed mutagenesis studies of the putative sites around those radicals. For Y_D, the hydrogen bond acceptor was predicted to be D2-H190 (H189 for *Synechocystis*) from sequence analysis[2a] and structural modeling.[22] Mutagenesis of this histidine residue in D2 produced marked changes in the EPR spectrum of the $Y_D^\bullet$ species[13,15] and a loss of the exchangeable proton feature in the ENDOR spectrum.[13] Mutagenesis of the corresponding histidine in the D1 polypeptide, however, left the EPR spectrum of the $Y_Z^\bullet$ radical essentially unaffected.[24,56]

Spin Densities in Tyrosyl Radicals. One of the key issues we sought to address in these studies was a comparison of the spin-density distribution in $Y_Z^\bullet$, relative to other tyrosyl radicals that have been characterized. The motivation for this derives from the fact that catalysis in tyrosyl radical-containing enzymes covers a broad range of reactions, and a potential means by which to direct this radical-initiated chemistry is to control the spin-density distribution in the radical. Warncke *et al.*[11] discussed factors that control ρ values in tyrosyl radicals and were able to eliminate β-methylene conformation and delocalized solvent interactions as significant factors in modulating the spin densities. They were, however, undecided as to the effect of hydrogen bonding, particularly in light of reported hydrogen bond modulation of the spin at the carbonyl oxygens in semiquinone radicals.[57] Table 2 compares the spin-density distribution for $Y_Z^\bullet$ to those for a variety of tyrosyl radicals that have been reported in the literature.[58] This comparison shows clearly that there is little variation in spin density among these radicals. At the ortho and meta positions, the densities are nearly constant for the six radicals. For the C_1 and C_4−O positions, there appears to be a somewhat greater deviation. For these, however, we consider the accuracy of the determinations to be ±0.03, which suggests that the apparent differences may not be significant. We conclude that the spin densities for the radicals in Table 2 are essentially indistinguishable.

Table 2. Spin Densities in Various Tyrosyl Radicals[a]

radical	C_1	C_2 (C_6)	C_3 (C_5)	C_4−O	ref
Y_Z	0.37	−0.07	0.26	0.25	this work
Y_D	0.37	−0.06	0.25	0.25	11
RNR	0.38	−0.07	0.26	0.24	37, 58
Y (glass)	0.34	−0.06	0.25	0.28	40, 48
Y (crystal)	0.32	−0.06	0.25	0.30	59
Y (solution)		−0.06	0.25		49

[a] See ref 39 for a discussion of the sign of the spin densities.

For the Y_{122} radical in ribonucleotide reductase, hydrogen bonding to the phenol oxygen has not been detected, whereas for $Y_D^\bullet$ and for the single-crystal tyrosyl radical, hydrogen bonds occur. For $Y_Z^\bullet$, as discussed above, we have not detected a well-ordered hydrogen bond by CW-ENDOR methods, although disordered hydrogen bonding appears likely.[21] The conclusion from Table 2, that the tyrosyl radical spin densities are only slightly different in these diverse samples, indicates that hydrogen bonding and/or electrostatic perturbation in the vicinity of the phenol oxygen has but little effect on ρ values. In addition, point mutations in the close vicinity of $Y_D^\bullet$ left the spin-density distribution of the radical essentially unaffected.[16] Tyrosyl radicals in proteins do not appear to be tuned to specific function by large-scale (>10%) modulation of their spin-density distribution by the local protein environment.

These results also have interesting implications for recent high-field EPR measurement of ***g***-tensors in tyrosyl radicals. Gerfen *et al.*,[60] for example, recently concluded that the differences that they observed in the ***g***-tensor component that lies along the C_1−C_4−O direction in the ribonucleotide reductase tyrosyl radical, relative to $Y_D^\bullet$, arose from a 30% difference in oxygen spin density for these two radicals. Our results show that this is not the case; if differences in ***g***-tensor components do correlate with phenol oxygen spin densities in tyrosyl radicals, then the correlation arises principally from hydrogen-

(56) Roffey, R. A.; van Wijk, K. J.; Sayre, R. T.; Styring, S. *J. Biol. Chem.* **1994**, *269*, 5115−5121.

(57) Feher, G.; Isaacson, R. A.; Okamura, M. Y.; Lubitz, W. In *Antennas and Reaction Centers of Photosynthetic Bacteria*; Michel-Beyerle, M. E., Ed.; Springer-Verlag: Berlin, **1985**; Chemical Physics 42, pp 174−189.

(58) For the tyrosyl radical in *E. coli* ribonucleotide reductase (RNR), Bender *et al.* [37] originally reported spin densities as follows: C_1 (0.49), $C_{2,6}$ (−0.07), $C_{3,5}$ (0.26), C_4 (−0.03), O (0.16). Hoganson and Babcock (unpublished results) have used ^{17}O labeling to test the oxygen spin density in RNR directly and have found a value of 0.29, significantly greater than that reported by Bender *et al.* Reexamination of the earlier analysis shows that Bender *et al.* assumed that the hyperfine coupling to the more weakly coupled β-methylene ^1H was purely dipolar. If this assumption is relaxed and an isotropic component for the hyperfine coupling to the weakly coupled β-^1H_W is calculated from the double-resonance peaks, then re-evaluation of the ENDOR data for the strongly and weakly coupled β-^1H shows that the spin density at C_1 will decrease to 0.38, which is consistent with the higher oxygen spin density found experimentally. The revised spin densities for RNR are included in Table 2.

(59) Fassanella, E. L.; Gordy, W. *Proc. Natl. Acad. Sci. U.S.A.* **1969**, *62*, 299−304.

(60) Gerfen, G. J.; Bellew, B. F.; Un, S.; Bollinger, J. M.; Stubbe, J.; Griffin, R. G.; Singel, D. J. *J. Am. Chem. Soc.* **1993**, *115*, 6420−6421.

bonding effects on excited-state energies rather than on ground-state spin densities.

Rotational Mobility and Conformation at the $Y_Z^\bullet$ Methylene Position. The ^{2}H-ESEEM spectra for the β-hydrogen interaction in $Y_Z^\bullet$ were analyzed by assuming a distribution of C_1-C_β rotamers. A ρ value of 0.37 ± 0.03 and $\Delta\theta$ of $\sim\pm7°$ were obtained from the constraints on the envelope modulation depths and the relative amplitudes of the β-^{2}H ν_α and $2\nu_\alpha$ features (Figure 7). The most probable dihedral angle for β-^1H_S is calculated to be 44° with a dihedral angle range $35° \leq \theta \leq 49°$. The corresponding values in β-^1H_W, obtained by assuming an idealized sp^3 hybridization at C_β (thus $\theta_2 = |\theta_1 - 120°|$), are 76° with a range $71° \leq \theta \leq 85°$. For the Y_D radical, the corresponding dihedral angles equal 52° and 68°, respectively. The mobility around the C_1-C_β bond of $Y_D^\bullet$ is greatly restricted, with the experimental uncertainty being ≤4°.[11] In contrast, the distribution in $Y_Z^\bullet$ C_1-C_β rotamers shows that $Y_Z^\bullet$ is rotationally mobile in the Mn-depleted samples we have studied.

The evidence of higher rotational mobility of $Y_Z^\bullet$ compared to $Y_D^\bullet$, as revealed by ESEEM on the β-^{2}H labeled samples in this work on $Y_Z^\bullet$ and in the earlier study on $Y_D^\bullet$,[11] is corroborated by the ENDOR spectra of unlabeled samples of both radicals in Figure 6. A distribution in dihedral angles results in a distribution in A_{iso} values for each β-^{1}H nucleus, which will broaden the ENDOR line shape. This is apparent in the spectrum of $Y_Z^\bullet$, particularly on the high-frequency side of the β-^1H_S feature, which does not overlap with the features arising from the 3,5-^{1}H. For $Y_D^\bullet$ in spinach, the ENDOR line shape of the β-^1H_S is narrower and sharper, thus indicating less spread in resonance frequencies and, consequently, lower rotational mobility around the C_1-C_β bond. For $Y_D^\bullet$ in *Synechocystis*, the situation is complicated by spectral overlap with the 3,5-^{1}H features. However, the slope on the high-frequency side of the β-^1H_S feature is clearly steeper for $Y_D^\bullet$ then for $Y_Z^\bullet$ indicating broadening of the β-^{1}H ENDOR line shape for the latter, consistent with the ESEEM analysis.

Attempts to evaluate the effects of rotational mobility on the ENDOR spectra quantitatively by spectral simulation are hampered by the fact that ENDOR intensities are a complicated function of electron and nuclear relaxation effects. Accordingly, we have not pursued these in detail; in this circumstance, the ESEEM data are more quantitatively informative. The effect of β-methylene rotational mobility on the ENDOR spectrum is to build intensity in the region around the most probable value of the isotropic coupling. This is evident in Figure 6 for $Y_Z^\bullet$ where a broad maximum is observed in the region around 29.4 MHz. This peak frequency corresponds to a hyperfine splitting of 30.2 MHz, which is close to the 31.0 MHz value derived from the ESEEM data. For the weakly coupled β-methylene ^{1}H, we expect similar manifestations of rotational mobility, that is, a buildup of intensity near its most probable isotropic coupling value. The 3.3-MHz splitting of the a′,a hyperfine transition in Figure 4, assigned to β-^1H_W, correlates well with the 3.5 MHz value obtained from the ESEEM analysis. Using the isotropic hyperfine couplings of 30.2 and 3.3 MHz, as derived from the ENDOR spectra and eq 2 above, we obtain a spin density at the C_1 carbon of 0.36, which is consistent with the value from the ESEEM analysis.

Two important conclusions emerge from considerations of the β-methylene couplings in $Y_Z^\bullet$ and $Y_D^\bullet$. First, the distinction between the two radicals, in terms of rotational mobility, extends to both procaryotic cyanobacteria and eucaryotic higher plant systems. The work reported here for $Y_Z^\bullet$, and earlier for $Y_D^\bullet$,[11] was carried out in the cyanobacterium *Synechocystis* and shows that $Y_Z^\bullet$ is motionally less confined than $Y_D^\bullet$ in this organism. Mino and Kawamori investigated Photosystem II in spinach and reported that $Y_Z^\bullet$ showed greater flexibility in its local protein interactions than $Y_D^\bullet$, as judged by the temperature dependence of the ENDOR spectra of the two radicals.[14] The relative rigidity of $Y_D^\bullet$ in spinach is confirmed here by the sharp, well-defined resonances for the strongly coupled β-^1H_S of this radical (Figure 6b). Second, we confirm earlier work by Barry and co-workers that indicated that, in *Synechocystis*, the hyperfine interaction with the more strongly coupled β-^1H_S is slightly greater in $Y_Z^\bullet$ than in $Y_D^\bullet$.[20b] The origin of this effect is a difference in most probable dihedral angles for the two radicals, as discussed above.

Dipolar Couplings in Tyrosyl Radicals. As described above, the isotropic hyperfine coupling allows one to estimate the unpaired spin-density distribution on the phenoxyl ring. An independent estimation of this distribution can be obtained by analysis of the dipolar couplings. This method was pioneered by McConnell and Strathdee[61] and has been applied to the tyrosyl radical in *E. coli* RNR.[37] This method is sensitive to assumptions about the sizes of the 2p orbitals, which are expressed as effective atomic numbers, and to the geometry of the radical. With the spin densities in Figure 8, reasonable values of the effective atomic numbers (3.0 and 3.4 for carbons carrying positive and negative spin density, respectively; 3.5 for oxygen), and a radical geometry from *ab initio* methods,[62] we calculate a set of tensor components for the ring ^{1}H that reproduces our observations in Table 1.

The dipolar splittings of the β-methylene hydrogens are due almost entirely to the spin at C_1. For a spin density of 0.37 and an effective atomic number of 3.0, we expect to observe $A_{||} - A_\perp$ of 7.0 MHz, which is substantially smaller than that calculated when the electron is assumed to be a point dipole. The strongly coupled β-^1H_S ENDOR resonance in $Y_D^\bullet$ (spinach) is spread over 3.5 MHz (i.e., $(A_{||} - A_\perp)/2$), consistent with its conformational immobility. The ENDOR resonance in $Y_Z^\bullet$ *(Synechocystis)* is broader and ranges over 6 MHz, as expected from its distribution in β-methylene group geometry.

Functional Implications of the Structure and Dynamics of $Y_Z^\bullet$. The prevailing model of the role of Y_Z in PSII is that it plays a simple electron-transfer function in interfacing the photochemistry that occurs at P_{680} to multielectron, water-splitting chemistry at the $(Mn)_4$ cluster (Scheme 1). By re-reducing P_{680}^+ in times short relative to the P_{680}^+/Q_A^- recombination time, $Y_Z^\bullet$ ensures high quantum efficiency in PSII. In recent years, our understanding of the factors that are critical in maximizing electron-transfer rates has developed considerably,[63] and if Y_Z were to function simply as a fast electron-transfer component, we would expect to see these implemented in the design of PSII. Thus, we would predict a short Y_Z-P_{680} distance and an environment and structure that minimize the reorganization energy λ during tyrosyl oxidation and reduction. Controlling these factors closely is especially critical in PSII, where the driving forces for the electron-transfer reactions that precede O_2 evolution are small (the total free energy drop between P_{680}^+ through Y_Z and $(Mn)_4$ to H_2O is less than 300 mV).

(61) McConnell, H. M.; Strathee, J. *Mol. Phys.* **1959**, *2*, 129–138.
(62) Chipman, D. M.; Liu, R.; Zhow, X.; Puley, P. *J. Chem. Phys.* **1994**, *100*, 5023–5035.
(63) (a) Marcus, R. A.; Sutin, N. *Biochim. Biophys. Acta* **1985**, *811*, 265–322. (b) Williams, J. In *Electron Transfer in Biology and the Solid State*; Johnson, M. K., King, B. R., Kurtz, D. M., Jr.; Kutal, C., Norton, M. L., Scott, R. A., Eds.; American Chemical Society: Washington, DC, 1990; Advances in Chemistry 226, pp 3-23. (c) Onuchic, J. N.; Beratan, D. N.; Winkler, J. R.; Gray, H. B. *Annu. Rev. Biomol. Struct.* **1992**, *21*, 349–377. (d) Moser, C. C.; Keske, J. M.; Warncke, K.; Farid, R. S.; Dutton, P. L. *Nature* **1992**, *355*, 796–802.

The distance constraint appears to be met, as a Y_Z/P_{680} separation of 7−12 Å has been estimated from EPR line-broadening measurements.[64] Minimization of λ occurs when the electron-transfer process takes place between donor/acceptor pairs in hydrophobic environments and when changes in structure about the cofactors upon oxidation/reduction are minimized.[63] Neither of these principles, however, appears to be in force for $Y_Z^\bullet$. Molecular modeling suggests that the Y_Z site is considerably more hydrophilic than is the Y_D site.[23] Moreover, the results presented here show that $Y_Z^\bullet$ is rotationally mobile and, in agreement with recent ENDOR[21] work, that $Y_Z^\bullet$ is not involved in a hydrogen bond with a specific and fixed O···H geometry. The hydrogen bond status of $Y_Z^\bullet$ and its rotational mobility contrast sharply with $Y_D^\bullet$, which is involved in a structurally well-ordered hydrogen bond and rotationally constrained;[11-13] a simple proton-rocking model accounts for the motion of its phenol proton upon redox change.[65] Thus, Y_D and its immediate environment appear to be designed to facilitate a pure electron-transfer function for this residue. For Y_Z, on the other hand, all three factors—hydrophilicity, rotational mobility, and lack of a well-ordered hydrogen bond—should increase λ substantially and decrease its effectiveness as a fast electron-transfer component.

These considerations suggest a role for Y_Z in PSII that extends beyond that of simple electron transfer. Several observations support this conjecture. First, early work on the re-reduction of $Y_Z^\bullet$ during S-state advance showed that water oxidation and O_2 evolution were rate-limited by the $S_3Y_Z^\bullet \rightarrow S_4Y_Z$ transition; formation of the oxygen−oxygen bond and O_2 release are fast, relative to the $S_3Y_Z^\bullet$ redox process.[9a] Second, it appears that the proton releases that necessarily occur during the water-splitting process primarily accompany the oxidation of Y_Z and take place upon each S-state transition.[66] This contrasts with earlier views in which these protolytic events were thought to occur asynchronously with S-state advance and to be associated with $Y_Z^\bullet$ reduction. Finally, electron magnetic-resonance results on the split S_3 signal recently reported by Gilchrist *et al.*[67] indicate that a redox-active tyrosine is in close proximity (~4.5 Å) to the $(Mn)_4$ cluster in PSII. The characteristics of this radical, both in terms of its hyperfine couplings to the β-methylene hydrogens and in terms of rotational mobility of its phenol head group, are similar to those we report here for $Y_Z^\bullet$ and are consistent with their identification of the tyrosyl radical with $Y_Z^\bullet$. This work also indicates that the characteristics we report here for Y_Z in the absence of the $(Mn)_4$ cluster persist in samples in which the metal center is preserved. As a caveat, however, we note that neither the work reported here nor that by Gilchrist *et al.*[67] has been carried out on PSII samples competent in O_2 evolution.

Scheme 2

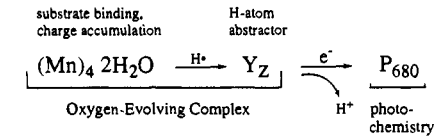

These observations place a deprotonated, rotationally mobile tyrosyl radical in close proximity to the $(Mn)_4$ cluster and implicate it in the rate-limiting steps of water-oxidation chemistry. Scheme 1 is inconsistent with these findings. Rather, PSII takes on characteristics similar to other radical-containing enzymes. In these systems, it has become apparent lately that a key role played by the radical in catalysis is hydrogen abstraction from substrate; moreover, a common theme is to locate the redox-active side chain in close proximity (< 10 Å) to a dioxygen-activating metal center.[68] The $Y_Z/(Mn)_4$ center has clear analogies to these systems and can be viewed as a member of the emerging family of radical-containing metalloenzymes. Scheme 2 shows a model that summarizes our view of the operation of the radical/metal-center complex in water oxidation.[69] In analogy to other radical enzymes, Y_Z and the $(Mn)_4$ cluster are envisioned as acting as a single entity in forming the Oxygen-Evolving Complex. Within this complex, the $(Mn)_4$ cluster acts to bind substrate water. $Y_Z^\bullet$, which has been deprotonated during its oxidation by P_{680}^+, abstracts hydrogen atoms from the bound substrate in a process that may be either sequential[70] or concerted.[71] In Scheme 2, $Y_Z^\bullet$ is postulated to carry out this process on each S-state transition; Gilchrist et al.[67] have proposed a similar mechanism from their work on the split S_3 signal. Deprotonation of Y_Z during its oxidation and reprotonation upon reduction are critical events in this mechanism and are likely to occur from different directions, which provides a rationale for the rotational mobility we observe. The oxidizing equivalents created in this process are ultimately delocalized in the $(Mn)_4$ cluster so that S-state advances conform to the conventional view of charge accumulation in the metal cluster.

Acknowledgment. We acknowledge valuable discussions with Professors Richard Debus, David Britt, and Charles Yocum. This work was supported by the Swedish Natural Science Research Council to S.S., by NIH Human Research Frontiers and USDA grants to G.T.B., by NRI/CGP/USDA to B.A.D., and by NIH to J.McC. C.T. gratefully acknowledges support from The Foundation BLANCEFLOR Boncompagni-Ludovisi, née Bildt.

JA951800Q

(64) (a) Bock, C. H.; Gerken, S.; Stehlik, D.; Witt, H. T. *FEBS Lett.*, **1988**, *227*, 141−146. (b) Hoganson, C. W.; Babcock, G. T *Biochemistry* **1989**, *28*, 1448−1454.

(65) Babcock, G. T.; Barry, B. A.; Debus, R. J.; Hoganson, C. W.; Atamian, M.; McIntosh, L.; Sithole, I.; Yocum, C. F. *Biochemistry* **1989**, *28*, 9557−9565.

(66) (a) Lübbers, K.; Haumann, M.; Junge, W. *Biochim. Biophys. Acta* **1993**, *1183*, 210−214. (b) Haumann, M.; Junge, W. *Biochemistry* **1994**, *33*, 864−872. (c) Bögerhausen, O.; Junge, W. *Biochim. Biophys. Acta* **1995**, *1230*, 177−185.

(67) Gilchrist, M. L., Jr.; Ball, J. A.; Randall, D. W.; Britt, R. D. *Proc. Natl. Acad. Sci. U.S.A.* In press.

(68) *Metal Ions in Biological Systems;* Sigel, H., Sigel, A., Eds.; Marcel Dekker: New York, **1994**; Vol. 30.

(69) A report that amplifies the details of this model will be published elsewhere (Hoganson, C. W.; Lydakis-Simantiris, N.; Tang, X.-S.; Tommos, C.; Warncke, K.; Babcock, G. T.; Diner, B. A.; McCracken, J.; Styring, S. *Photosynth. Res.* In press).

(70) Foti, M.; Ingold, K. U.; Lusztyk, J. *J. Am. Chem. Soc.* **1994**, *116*, 9440−9447.

(71) Savéant, J.-M. *Acc. Chem. Res.* **1993**, *26*, 455−461.